

Minerva Access is the Institutional Repository of The University of Melbourne

Author/s:

Voermans, JJ;Liu, Q;Marchenko, A;Rabault, J;Filchuk, K;Ryzhov, I;Heil, P;Waseda, T;Nose, T;Kodaira, T;Li, J;Babanin, AV

Title:

Wave dispersion and dissipation in landfast ice: Comparison of observations against models

Date:

2021-12-10

Citation:

Voermans, J. J., Liu, Q., Marchenko, A., Rabault, J., Filchuk, K., Ryzhov, I., Heil, P., Waseda, T., Nose, T., Kodaira, T., Li, J. & Babanin, A. V. (2021). Wave dispersion and dissipation in landfast ice: Comparison of observations against models. *Cryosphere*, 15 (12), pp.5557-5575. <https://doi.org/10.5194/tc-15-5557-2021>.

Persistent Link:

<https://hdl.handle.net/11343/308682>

License:

[CC BY](#)



Wave dispersion and dissipation in landfast ice: comparison of observations against models

Joey J. Voermans¹, Qingxiang Liu^{2,1}, Aleksey Marchenko³, Jean Rabault^{4,5}, Kirill Filchuk⁶, Ivan Ryzhov⁶, Petra Heil⁷, Takuji Waseda⁸, Takehiko Nose⁸, Tsubasa Kodaira⁸, Jingkai Li², and Alexander V. Babanin^{1,9}

¹Department of Infrastructure Engineering, University of Melbourne, Parkville, Australia

²Physical Oceanography Laboratory, Ocean University of China, Qingdao, China

³Arctic Technology Department, The University Centre in Svalbard, Longyearbyen, Norway

⁴Norwegian Meteorological Institute, Oslo, Norway

⁵Department of Mathematics, University of Oslo, Oslo, Norway

⁶Arctic and Antarctic Research Institute (AARI), St. Petersburg, Russian Federation

⁷Australian Antarctic Division and Australian Antarctic Program Partnership, University of Tasmania, Hobart, Australia

⁸Graduate School of Frontier Sciences, The University of Tokyo, Kashiwa, Chiba, Japan

⁹Laboratory for Regional Oceanography and Numerical Modeling, National Laboratory for Marine Science and Technology, Qingdao, China

Correspondence: Joey J. Voermans (jvoermans@unimelb.edu.au)

Received: 12 July 2021 – Discussion started: 22 July 2021

Revised: 15 October 2021 – Accepted: 15 November 2021 – Published: 10 December 2021

Abstract. Observations of wave dissipation and dispersion in sea ice are a necessity for the development and validation of wave–ice interaction models. As the composition of the ice layer can be extremely complex, most models treat the ice layer as a continuum with effective, rather than independently measurable, properties. While this provides opportunities to fit the model to observations, it also obscures our understanding of the wave–ice interactive processes; in particular, it hinders our ability to identify under which environmental conditions these processes are of significance. Here, we aimed to reduce the number of free variables available by studying wave dissipation in landfast ice. That is, in continuous sea ice, such as landfast ice, the effective properties of the continuum ice layer should revert to the material properties of the ice. We present observations of wave dispersion and dissipation from a field experiment on landfast ice in the Arctic and Antarctic. Independent laboratory measurements were performed on sea ice cores from a neighboring fjord in the Arctic to estimate the ice viscosity. Results show that the dispersion of waves in landfast ice is well described by theory of a thin elastic plate, and such observations could provide an estimate of the elastic modulus of the ice. Observations of wave dissipation in landfast ice are about an order

of magnitude larger than in ice floes and broken ice. Comparison of our observations against models suggests that wave dissipation is attributed to the viscous dissipation within the ice layer for short waves only, whereas turbulence generated through the interactions between the ice and waves is the most likely process for the dissipation of wave energy for long periods. The separation between short and long waves in this context is expected to be determined by the ice thickness through its influence on the lengthening of short waves. Through the comparison of the estimated wave attenuation rates with distance from the landfast ice edge, our results suggest that the attenuation of long waves is weaker in comparison to short waves, but their dependence on wave energy is stronger. Further studies are required to measure the spatial variability of wave attenuation and measure turbulence underneath the ice independently of observations of wave attenuation to confirm our interpretation of the results.

1 Introduction

When waves propagate from open water into sea ice, their energy decays at a rate as determined by the properties of

the sea ice (e.g., Shen, 2019; Squire, 2020). To model the propagation of wave energy into the ice cover of the polar seas, the impact of the ice on the wave energy balance in wave forecasting models is typically formulated in terms of an ice damping source term S_{ice} which, when wave scattering is assumed to be insignificant and wave dissipation processes are approximated as linear, is given by (e.g., Shen, 2019)

$$S_{\text{ice}} = -\alpha c_g E, \quad (1)$$

where α is the apparent spatial attenuation rate, c_g is the group velocity (and can be determined from the wave dispersion relationship), and E is the wave energy density. Both α and c_g are strongly dependent on the local wave and ice properties. Evidently, following Eq. (1), α and c_g are fundamental variables which require parameterizations based, preferably, on the physics that underpin the relevant wave–ice interactive processes.

Most of the dissipative processes describing the change of wave energy into the ice cover can be organized in two categories: those that attribute wave energy dissipation to (i) the properties of the ice layer, such as viscous (e.g., Weber, 1987) and viscoelastic theory (e.g., Squire and Allan, 1977; Wang and Shen, 2010), and (ii) viscous or turbulent kinetic energy dissipation in the water surrounding the ice, such as bottom friction (e.g., Kohout et al., 2011; Voermans et al., 2019), overwash (e.g., Toffoli et al., 2015; Nelli et al., 2020) and floe–floe interactions (e.g., Rabault et al., 2019) (we refer to Squire, 2020; Shen, 2019; Collins et al., 2017, for a comprehensive overview on wave–ice interaction processes). Each of these processes relies, one way or another, on the physical and material properties of the ice. Sea ice is, however, a complex medium and can consist of a mixture ice types (e.g., frazil and consolidated ice), different length scales (from pancake ice to a continuous ice sheet), and even within each type the material properties of each element can vary greatly (e.g., first-year versus multi-year ice). As each physical and material detail of the ice can have a leading impact on the transformation of the wave field, capturing such variability at global scales for modeling purposes is challenging.

A common approach in tackling this obstacle is by treating the sea ice as a continuum; that is, it is assumed that the ice can be represented by a homogeneous ice layer with “effective” ice properties rather than measurable material properties. The effective properties are then, ultimately, a function of the ice layer characteristics. Thus, if the effective properties of the ice are known, the development of waves in ice (i.e., α and c_g) can be modeled at macroscopic scales. The calibration of these continuum models against in situ and satellite observations has been the topic of many studies on wave–ice interactions (e.g., Ardhuin et al., 2016; Cheng et al., 2017, 2020). However, a critical problem with this approach is that all models can, to a certain degree, be fitted to the observations even if the physical process upon which the model was founded is of no relevance in the environmental

setting. It is perhaps for this reason that there is still a very limited understanding of how much each dissipative process actually contributes to the total dissipation rate under any given ice and wave conditions. Instead, our current practical understanding of the wave attenuation rate tends to be restricted to the power dependency of the wave attenuation rate α with wave frequency f^n , where n tends to vary between 2 and 4 (Meylan et al., 2018), which, in turn, gives us clues as to which processes could be of importance (Rogers et al., 2021).

Rather than attempting to parameterize the effective properties of the models for different ice conditions, a new perspective on the functioning of models and theories may be provided when near-homogeneous ice conditions are studied (realistically, the ice layer is never perfectly homogeneous). For example, when a continuous ice sheet is considered, such as landfast ice, the effective properties of the ice layer as per the continuum model should revert to the material properties of consolidated ice which, theoretically, may be measured independently. This then reduces the number of free variables available to fit models to observations. However, in situ observations of wave–ice interactions in landfast ice are rare, with the notable exceptions of Squire et al. (1994), Sutherland et al. (2019), and Kovalev et al. (2020). Therefore, to provide further insights into the wave–ice interactive processes that could play a dominant role in the transformation of waves propagating in sea ice, we performed two field experiments on landfast ice. Specifically, the ice motion was recorded over the duration of a few weeks on landfast ice in the Arctic and Antarctic. The observations are used to determine the wave attenuation rates and estimate the dispersion relationship in a continuous ice sheet, and the results are compared against available theories and models. To support our comparison against contemporary wave dissipation models, we use estimates of sea ice viscosity obtained from laboratory tests on sea ice cores taken from a neighboring fjord at the time of our Arctic field experiments.

2 Methods

2.1 Field experiments

Two field experiments were performed on landfast ice to measure the wave-induced ice motion, one in the Arctic, and the other in the Antarctic. In both experiments, open-source ice motion loggers were used (Rabault et al., 2020), hereafter referred to as “ice buoys”. The ice buoys recorded ice motion using a high-accuracy inertial motion unit (IMU, VectorNav VN-100) at a frequency of 10 Hz and transmitted the full wave spectrum, geographical location, and battery status, every 2:45 and 4:15 h for the Arctic and Antarctic experiment, respectively, through Iridium connectivity.

In the Arctic experiment, three ice buoys were deployed along the main axis of Grønfjorden, Svalbard, with the first

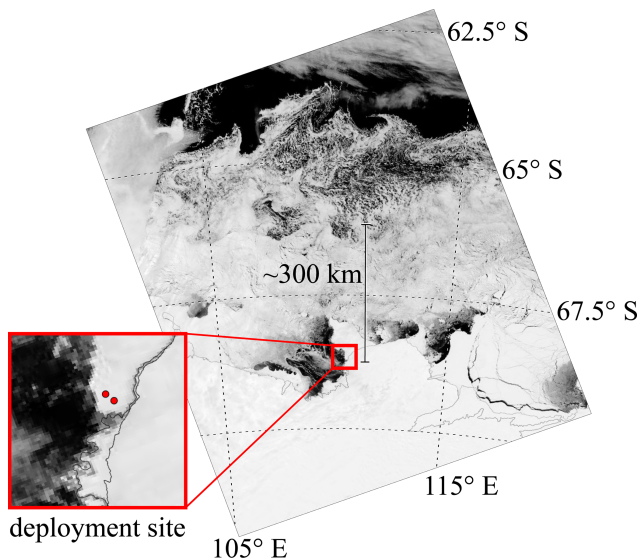


Figure 1. MODIS imagery (<https://worldview.earthdata.nasa.gov/>, last access: 7 May 2021) of the deployment site and sea ice on 10 November (end of deployment with clear sky). Instruments were deployed on landfast ice, and the site was separated from the Southern Ocean open water by a vast stretch of pack ice throughout the deployment.

buoy deployed approximately 500 m from the unbroken ice edge. The other two buoys were deployed 600 and 1300 m from the first buoy. Ice thicknesses of 0.3–0.4 m were measured at the start of the experiment. Instruments were deployed for approximately 2 weeks, after which they were retrieved. The maximum significant wave height measured (defined as $H_s = 4(\int E(f)df)^{1/2}$) was approximately 10 cm. Wind speed was not measured at the deployment site; however, based on measurements at Isfjord Radio the wind speed during the experiment is expected to have varied between 0–22 m s⁻¹. Time series of the significant wave height and peak period are shown for reference in Fig. A1a and are taken from Voermans et al. (2020). The reader is referred to this reference for more details of the Arctic experiment.

In the Antarctic experiment, two ice buoys were deployed on landfast ice north of Casey Station (66.2° S, 110.6° E; see Fig. 1) and positioned about 1.9 km apart. The buoys were deployed in October 2020 and retrieved after 3–4 weeks. During the experiment, 200–300 km of highly concentrated pack ice and a variable region of about 100 km of loosely packed ice (the marginal ice zone) separated the buoys from the Southern Ocean open water. As a result, only limited wave energy was measured during the experiment with significant wave height up to about $H_s = 3$ cm (Fig. A1b). The ice thickness was 1.1 m before and 1.3 m after the experiment. The local water depth at the deployment site was unknown but has been estimated, based on the wave dispersion relationship, at about 120 m.

There were no mechanical tests performed on local sea ice in either of the field experiments. However, at the time of the Arctic experiment, mechanical tests were performed through an independent project in a neighboring fjord to estimate sea ice viscosity. This experiment is summarized in Sect. 2.3, and, together with observations taken from literature, will serve as a proxy of the ice viscosity used in the comparison against various wave attenuation models. The methods and results of the mechanical tests and estimation of the ice viscosity are provided in Appendix B.

2.2 Data processing

Heave spectra were derived from the vertical acceleration spectra $E_A(f)$ as per $E(f) = 1/\omega^4 E_A(f)$, where $\omega = 2\pi f$. Examples of spectra are shown in Fig. A2. To avoid spurious results by instrument noise, we here use a signal-to-noise ratio (SNR) ≥ 2 as the threshold of acceptable data (e.g., Thomson et al., 2021). The noise level of the IMU was determined by fitting a power relationship through the high-frequency range of the spectrum $E(f)$ where no wave energy is expected or observed. The noise level is then removed from the spectra.

To determine the wave dispersion relation in ice, the wave number is estimated from the measurements of heave, pitch, and roll:

$$k(f) \approx \sqrt{\frac{E_\alpha(f) + E_\beta(f)}{E(f)}}, \quad (2)$$

where E_α and E_β are the spectra of the roll and pitch motion, respectively (Kuik et al., 1988; Collins et al., 2018). The Arctic experiment provided 110 estimates of $k(f)$. Similar to Collins et al. (2018), we notice an average bias of approximately 3 % for k/k_{ow} for the lower wave frequencies, e.g., for wave periods between 8 and 12 s, where k_{ow} is the wave number in open water. As the observed wave energy in the Antarctic experiment is significantly smaller than in the Arctic experiment, fewer data passed the signal-to-noise ratio (SNR) threshold criterion. A total of 38 spectra passed quality control; however, the number of valid observations within individual frequency bands varied between 3 and 19.

To estimate the dissipation of wave energy by sea ice, we assume that the spatial dissipation rate is well described by an exponential function (e.g., Wadhams et al., 1988):

$$E(f, x) = E(f, 0)e^{-\alpha x}, \quad (3)$$

where x is the distance of wave propagation into the ice pack. Equation (3) implicitly assumes that the dissipative processes are linear; i.e., the rate of energy dissipation is independent of the wave energy or wave amplitude (e.g., Squire, 2018). Evidently, this is not the case for all dissipative processes, such as turbulence (Herman, 2021; Voermans et al., 2020; Stopa et al., 2016; Kohout et al., 2011). Nevertheless, due to its simplicity and limitations in the field measurement campaigns, we adopt Eq. (3) as a first-order approximation of the

wave attenuation rate α . The buoys did not always measure at the same time due to variable quality of satellite connectivity causing a drift in the starting time of each record. For this analysis we therefore only consider data pairs obtained within $\Delta t = 30$ min of each other.

In Eq. (3) it is assumed that the direction of wave propagation is aligned with the axis of the buoy pair. In the case of the Arctic experiment, this seems a reasonable assumption as the buoys are aligned with the main axis of the fjord. For the Antarctic experiment, this assumption was tested using ERA5 re-analysis data in the open water just north of the marginal ice zone, indicating a relative bearing of approximately 15° with respect to the peak wave direction. As we do not have in situ observations of the wave directions (ideally the directional wave spectrum), and the estimated attenuation rate would be increased by less than 5% for a relative bearing of 15° , we did not correct for this misalignment. We further remove records where more than 25% of the frequency bands have a negative attenuation rate. We note that for the Arctic experiment only those observations are used that were obtained from the buoy pair furthest apart as they were deemed most accurate (see further discussion in Sect. 4). Implementing these additional criteria leaves nine profiles of the wave attenuation rate for the Arctic experiment and just two for the Antarctic experiment.

2.3 Ice viscosity

To compare our observations of wave attenuation against viscoelastic models, viscosity input is required. As no straightforward method is available to measure the viscosity of solid ice through field or laboratory experiments, the material is often simplified as a spring-dashpot model through which the viscosity can be estimated by stress-strain tests on a material sample. Estimates of the ice viscosity are, nevertheless, extremely rare. Tabata (1958) and Lindgren (1986) estimated an ice viscosity using a Maxwell–Voigt spring-dashpot model of 10^{13} Pa s $^{-1}$ (for sea ice at -10°C) and $\sim 6 \times 10^{10}$ Pa s $^{-1}$ (freshwater ice at about -5°C), respectively, whereas more recently the viscosity of laboratory-grown solid (salt water) ice was estimated to vary between 10^8 and 10^9 Pa s $^{-1}$ (Marchenko et al., 2020, 2021). While it is outside the scope of this study to provide a review on this topic, it is important to stress that different spring-dashpot models may produce different estimates of the ice viscosity.

In March 2020, a separate field measurement campaign was performed in the Van Mijen Fjord, Svalbard, to measure and estimate the material properties of naturally grown sea ice. Importantly, these measurements were done during the same period as the Arctic field experiment performed as described in Sect. 2.1, albeit in a different fjord in Svalbard. In addition to in situ cantilever experiments, vertical and horizontal ice cores were taken and tested in the laboratory. Distinction was made between columnar and sea spray ice. By describing the ice as a Burgers material (Maxwell–

Voigt spring-dashpot model), the viscosity coefficients were obtained through the estimation of the stress relaxation and elastic lag timescales (Marchenko et al., 2020, 2021). The estimate of the solid ice viscosity was $\mu_i = 3.2 \times 10^{10}$ and 3.9×10^{10} Pa s $^{-1}$ for the columnar sea ice cores and 3.0×10^{10} Pa s $^{-1}$ for the sea spray ice cores (note that the kinematic viscosity ν_i is related to the dynamic viscosity as $\nu_i = \mu_i/\rho_i$, where ρ_i is the ice density). For clarity, we use subscripts “i” and “w” to denote ice and water variables, respectively. Details on this approach and the coefficients obtained from the tests are provided in Appendix B.

Even though the (few available) estimates of consolidated ice viscosity vary by 5 orders of magnitude, 10^8 – 10^{13} Pa s $^{-1}$, it does provide critical insight into the approximate bounds for the viscosity of consolidated ice. In this study, we will use this range of μ_i to study the performance of viscoelastic models against our observations.

3 Results

The estimated dispersion relation for each experiment is shown in Fig. 2. By averaging in time and across instruments, we inherently assume that the ice conditions were constant across the deployment sites and remained unchanged over the duration of the experiments. A lengthening of the short waves is observed in both experiments. The consistent deviation from the open water dispersion relationship for the short waves suggests that the ice was indeed continuous and not broken (Sutherland and Rabault, 2016).

Observations are compared against the modeled dispersion relationship of a thin elastic plate for different values of the elastic modulus Y (Eq. C8, Liu and Mollo-Christensen, 1988). For the Arctic experiment, the average of k estimates corresponds well to the modeled dispersion relation with $Y = 4 \times 10^9$ Pa. For $f \approx 0.2$ Hz, the average value of k deviates from this line yet is well within the range of uncertainty given the limited number of observations at this frequency. Although this value Y is about twice as large as that estimated based on the measured ice salinity, water, and air temperature (Voermans et al., 2020), it is well within the general range of uncertainty of observations of Y (Timco and Weeks, 2010). For the Antarctic experiment, considerably fewer observations are available, resulting in larger scatter of the mean estimate of k . Nevertheless, observations correspond reasonably well to the modeled relationship using $Y \approx 2.5 \times 10^9$ Pa. As the ice thickness in the Antarctic experiment is 3–4 times larger than in the Arctic experiment, the lengthening of waves in the Antarctic experiment seems to become significant at about $f \gtrsim 0.1$ Hz, in contrast to $f \gtrsim 0.16$ Hz in the Arctic experiment.

The mean wave attenuation rate observed in the Arctic experiment decays with an increase in wave period (Fig. 3a) (except for $T = 17$ s, which was discarded from further analysis due to limited data points). As only two wave attenua-

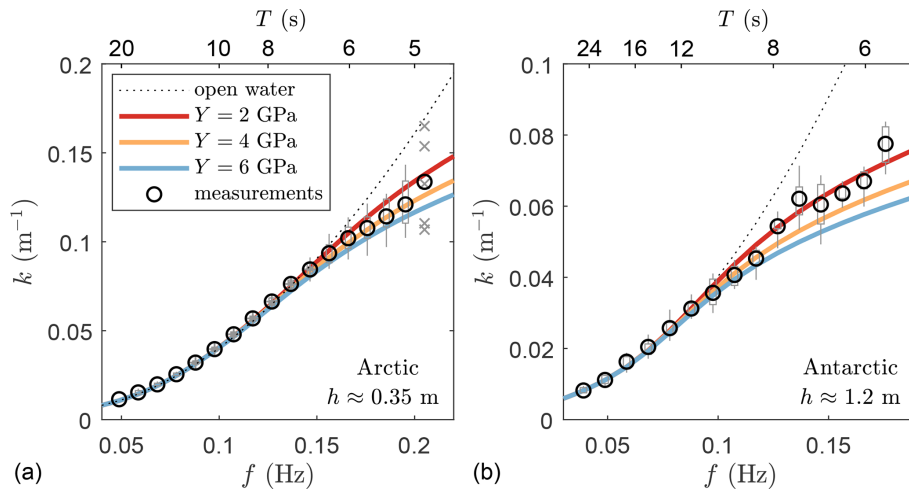


Figure 2. Mean values of the estimated wavenumber k in landfast ice based on experimental observations (circle) in (a) the Arctic and (b) the Antarctic. Solutions of the dispersion relation following an elastic thin plate are provided in color. Note that for the Arctic experiment there are only a limited number of observations available at $f = 0.21$ Hz (cross). In (a) and (b), boxes identify the 25th and 75th percentiles, the vertical bars identify the 9th and 91st percentiles, and circles identify the bin-averaged values.

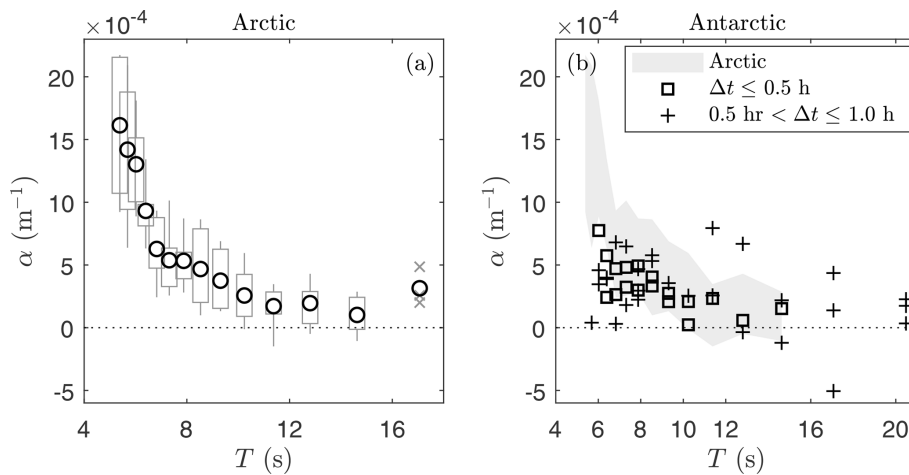


Figure 3. (a) Mean wave attenuation rate α as observed in the Arctic (circle), boxes identify the 25th and 75th percentiles, and the vertical bars identify the 9th and 91st percentiles. Note that the number of observations for $T = 17$ s in the Arctic experiment (cross) is limited. (b) Observations of the wave attenuation rate in the Antarctic with time difference between co-located buoy measurements below 0.5 h (square) and between 0.5 and 1.0 h (plus). Given the limited number of observations, no mean values are provided for the Antarctic experiment; however, the magnitude of the observations corresponds well with those observed in the Arctic.

tion profiles of our Antarctic experiment passed the quality control criteria, as outlined in Sect. 2.2, there are insufficient data available to reliably determine a mean wave attenuation rate for this experiment. Nevertheless, these observations are presented here as the little data available do seem to suggest that the wave attenuation rate is of the same order of magnitude as that observed in our Arctic experiment (Fig. 3b). Clearly, loosening the quality control criterion of $\Delta t \leq 0.5$ to 1 h greatly increases the scatter and thus the uncertainty of the wave attenuation observations.

As suggested by Rogers et al. (2016) and Shen (2019), the ice type (whether at the micro- or macroscopic level) is

perhaps the main determinant of the wave energy dissipation by the action of sea ice. In Fig. 4 our observations of wave dissipation in landfast ice (Arctic experiment only) are compared against those observed in other ice types including grease ice (Kodaira et al., 2020), pancake ice (Thomson et al., 2018), and pack ice (Kohout and Williams, 2013). We note that all observations in Fig. 4 are averages per experiment, and for the experiments of Kohout and Williams (2013) and Thomson et al. (2018), experiment-averaged estimates were retrieved from Liu et al. (2020). While within each experiment the magnitude of α can vary, the average values observed in pack ice are an order of magnitude smaller than

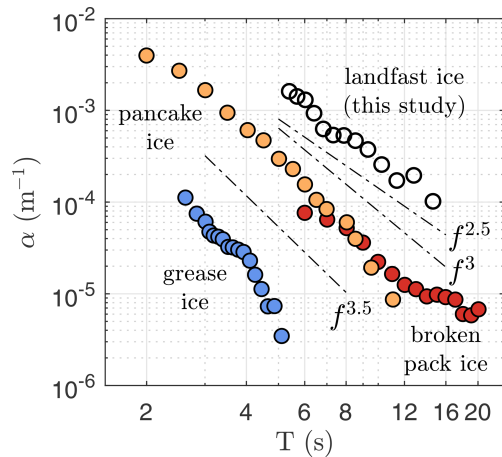


Figure 4. Comparison of experiment-averaged wave attenuation rates α for different types of sea ice (all field observations): grease ice (Kodaira et al., 2020), broken pack ice (Kohout and Williams, 2013), pancake ice (Thomson et al., 2018) and landfast ice (this study). Mean attenuation values of the experiments of Kohout and Williams (2013) and Thomson et al. (2018) are taken from Liu et al. (2020). Observations of α in landfast ice fall between $f^{2.5}$ and f^3 .

what we observe in landfast ice for $5 \leq T \leq 16$. Such a difference was also observed by Collins et al. (2015) and Ardhuin et al. (2020), who suggest that the wave attenuation is dominated by whether the ice is broken or unbroken. For our observations of α in landfast ice, we observe a power regime between $f^{2.5}$ and f^3 .

In Fig. 5 our Arctic wave attenuation observations are compared against different wave dissipation models (an overview of the models is provided in Appendix C). Two processes are considered here: attenuation attributed to the ice layer (cool color tones in Fig. 5) and to the water body (warm color tones). To compare our observations against viscoelastic models, both the elastic modulus and viscosity of the ice need to be known. While we have an estimate of the elastic modulus of ice during the experiment (i.e., Fig. 2a), the viscosity is unknown. We compare our observations against two different viscoelastic models, the first is that of Squire and Allan (1977), simplified to a Voigt model (Li et al., 2015; Sree et al., 2018). The lower bound value of the ice viscosity is used here, $\mu_i \in [10^8, 10^9]$, to match the observations. We note that this model provides nearly identical results for the ice parameters used in this study to that of Wang and Shen (2010). For $T < 7$ s, the viscoelastic model provides attenuation estimates of the same order of magnitude as our observations; however, for longer wave periods, there is a significant discrepancy in both slope and magnitude. The second viscoelastic model used is that of Marchenko et al. (2020, 2021), which is based on a linear Maxwell–Voigt model. The attenuation rates behave similarly to the model of Squire and Allan (1977), but with a significantly different order of magnitude. Unlike the viscoelastic model of Squire and Allan

(1977), a viscosity value of $\mu_i \in [10^{10}, 10^{11}]$ is required to match the short wave period observations of wave attenuation. We note that this viscosity range corresponds very well to the ice viscosity estimated through independent ice tests in a neighboring fjord (see Sect. 2.3). Fundamentally different from the model of Squire and Allan (1977) is that the model of Marchenko et al. (2020, 2021) is inversely proportional to the ice viscosity; that is, the wave attenuation decreases with an increase in ice viscosity. For the two-layer model of Sutherland et al. (2019), we have assumed a no-slip condition $\Delta_0 = 1$ at the water–ice interface. While there is no physical guidance as to what ϵ (the relative thickness of the wave-permitting ice layer) should be for a solid ice cover, we expect this to be small and thus adopted a value of $\epsilon = 0.01$. This leads to a strongly underestimated attenuation rate compared to the observed attenuation. The third model related to the ice layer properties is that of Marchenko and Cole (2017), which considers that wave energy is dissipated by brine migration induced by the flexural motion of the ice layer. As supported by the measurements of Golden et al. (2007), sea ice can be considered permeable when ice temperature is greater than about -5°C , and thus, the pumping of brine due to flexural deformations of ice is possible only near the bottom of the ice where the ice temperature is relatively high. This model, however, leads to an overestimation of the attenuation rate and a much stronger dependency of α on the wave frequency f .

The weakest form of wave attenuation by under-ice friction is through the development of a laminar boundary layer under the ice. Comparison against the model of Liu and Mollo-Christensen (1988), with $\nu_w = 1.8 \times 10^{-6}$, shows an underestimation of the dissipation rate by 2 orders of magnitude. To match the observations, the viscosity of the water needs to be increased to an effective value of $\nu_w = 10^{-2} \text{ m}^2 \text{ s}^{-1}$. While this is a common approach, caution is required in replacing the molecular viscosity by an effective viscosity as the physical problem stipulated by Liu and Mollo-Christensen (1988) considers a laminar boundary layer only. Using an effective viscosity, the slope reasonably matches the observations for $8 < T < 15$, whereas the attenuation rate is underestimated for shorter wave periods. Perhaps a more sophisticated way to include the effects of turbulence dissipation is through the model of Stopa et al. (2016), which is based on the analogy with the wave bottom boundary layer. However, with an arbitrary chosen roughness height of $z_0 = 0.01$ m, the modeled attenuation rate underestimates the observed dissipation rate considerably. Even increasing the friction factor to the limit value of $f_w = 0.3$ still shows an underestimation by an order of magnitude. The last model evaluated is that of Kohout et al. (2011), where the friction at the wave–ice interface is defined by a drag coefficient. To match the observations, we use a $C_D = 1$. While the fit is reasonable, the model of Kohout et al. (2011) has a slightly larger slope than that observed in the Arctic ex-

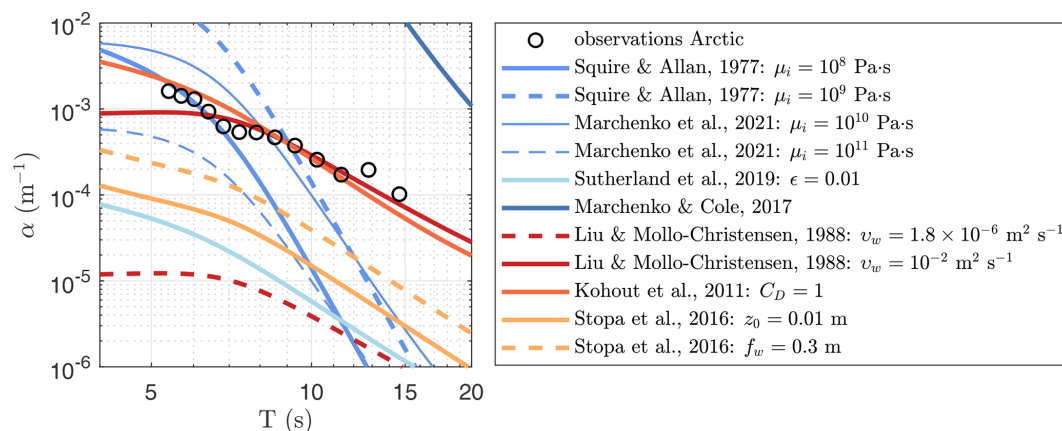


Figure 5. Comparison of wave attenuation rate α observed in the Arctic experiment against various wave dissipation models. These include models where dissipation is attributed to the ice layer (cool colour tones; Squire and Allan, 1977; Sutherland et al., 2019; Marchenko and Cole, 2017) and friction (warm colour tones; Liu and Mollo-Christensen, 1988; Kohout et al., 2011; Stopa et al., 2016).

periment but matches the observations well across the whole range of observed wave periods.

4 Discussion

Our observations of wave attenuation in landfast ice were compared against a variety of models. We find that viscoelastic theory cannot explain the attenuation rates observed in our Arctic experiment completely. Specifically, the power dependence of α on wave frequency is greatly overestimated for long wave periods (e.g., Meylan et al., 2018; Liu et al., 2020). However, for the shortest waves, the trend and magnitude tend to align well with the observations.

The model that performs comparatively well is the laminar boundary layer model of Liu and Mollo-Christensen (1988) using an effective viscosity of $10^{-2} \text{ m}^2 \text{ s}^{-1}$. If deemed correct, this would imply that the boundary layer under the ice is fully turbulent rather than laminar. Unlike our observations, the model of Liu and Mollo-Christensen (1988) shows a flattening of the attenuation rate for high frequencies, typically referred to as the rollover effect and attributed to local wind input and/or non-linear energy transfer (e.g., Li et al., 2017; Thomson et al., 2021). However, given that the ice cover is continuous here and the distance between the ice buoys is relatively small compared to the typical wave length, we do not expect any rollover effect in our experiments. While the required increase in ν_w to ν_t seems extraordinary, McPhee and Martinson (1994) and Marchenko et al. (2017) did observe, based on measurements under drifting ice, a similar eddy viscosity of $\nu_t = O(10^{-2})$. Yet, in those experiments, it is more likely that the observed turbulence was generated through the relative velocity between the drifting ice and the water rather than the wave orbital motions. Specifically, if one would estimate the magnitude of ν_t during our Arctic experiment as being the product of the

orbital wave velocity, $O(0.01 \text{ m s}^{-1})$, and the wave boundary layer thickness, $O(0.01 \text{ m})$ (that is, the product of the velocity scale and length scale of the largest turbulent eddies generated in the wave boundary layer), we would expect a maximum eddy viscosity of $\nu_t = O(10^{-4} \text{ m}^2 \text{ s}^{-1})$ instead. Nevertheless, the presence of more complex under-ice roughness, such as ice ridges and platelet ice, could significantly increase the eddy viscosity through increased under-ice surface roughness. However, without in situ observations of such features, the true eddy viscosity remains uncertain during our experiment.

The relatively simple model of Kohout et al. (2011) works reasonably well across the whole range of observed frequencies if a drag coefficient of $C_D = 1$ is used. Observations of the under-ice drag coefficient are rare, and those reported are often related to currents rather than waves. For currents under the ice, the largest values of the drag coefficient reported are $C_D = O(0.01\text{--}0.1)$ (Lu et al., 2011). However, when considering waves rather than currents, $C_D = 4$ has been considered by Herman et al. (2019), whereas Voermans et al. (2019) suggest that the drag coefficient increases exponentially with ice concentration. Extrapolation of their observations to a continuous ice cover gives $C_D = O(1\text{--}10)$, which, though highly speculative, makes $C_D = 1$ here not implausible.

A critical difference between the dissipative processes of the viscous ice layer and friction at the water–ice interface is that, to the first order, the former depends on ice thickness and not on the local wave height, whereas the latter scales with the wave height while being only weakly dependent on the ice thickness. Ice thickness is a second-order effect for wave attenuation by boundary layer turbulence as transfer of momentum to the ice is fundamentally determined by the surface roughness properties of the ice and the hydrodynamics below the ice. Only when second-order effects are considered, such as the impact of ice on the dispersion relation and a possible correlation between under-ice roughness and

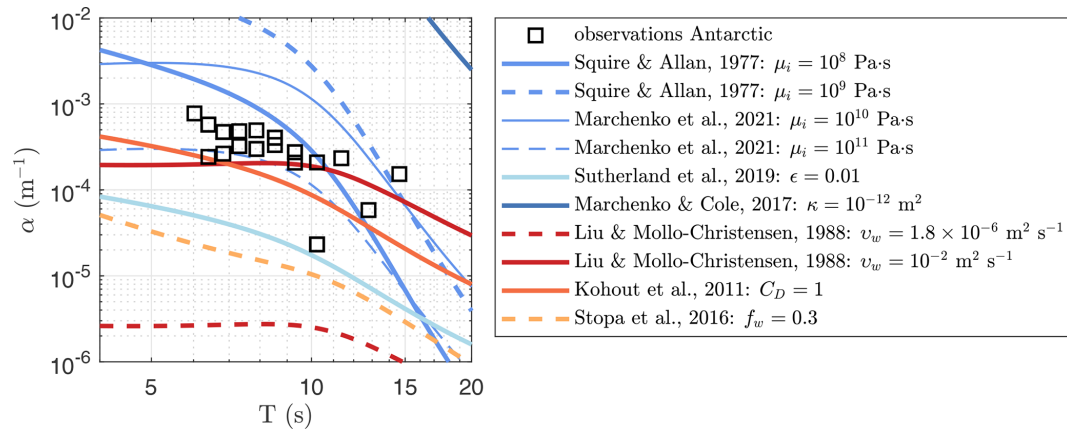


Figure 6. Same as Fig. 5, except for the Antarctic experiment. Models have not been fitted to the data. Note, limited observations are available for the Antarctic experiment, and results should be interpreted by their order of magnitude rather than fine-scale details.

ice thickness, can the ice thickness impact the wave attenuation rate by friction. Considering the first-order effects to be dominant, the estimated wave attenuation rates from the Antarctic experiment can provide some insight into the relative importance of the two dissipative processes as the ice thickness was 3–4 times larger whereas the maximum wave height was 2–3 times smaller than in the Arctic experiment. In Fig. 6 the Antarctic observations are compared against the same models, except here $Y = 2.5 \times 10^9$ Pa, $h = 1.2$ m, and $H_s \approx 0.03$ m, while assuming that the viscosity of the ice and under-ice drag coefficient remain the same. It is important to stress that the comparison of the Antarctic observations of α against the models is speculative, as we have insufficient observations available to determine the mean wave attenuation rate for this experiment. If one would assume the limited Antarctic observations to be representative for the experiment, the viscoelastic model of Squire and Allan (1977) now overestimates the observations by a factor of 3, whereas the boundary layer model of Kohout et al. (2011) underestimates the observations by a factor of 2. The viscoelastic model of Marchenko et al. (2020, 2021) captures the Antarctic field observations well, even if the same ice viscosity values are used as those derived in the Arctic. Unlike the model of Squire and Allan (1977), the attenuation rates of the model of Marchenko et al. (2020, 2021) become constant for $T < 7$ s under the ice conditions in the Antarctic experiment. Thus, taking into consideration the uncertainty in parameterizations and the observations, both under-ice friction and viscoelastic theory could explain the wave dissipation here.

Even though the friction models alone can reasonably replicate the observations of attenuation in both experiments, it is very plausible that both processes are of importance, albeit at different frequency ranges. The point at which the effective viscosity model of Liu and Mollo-Christensen (1988) and Kohout et al. (2011) starts to flatten, around $6 \leq T \leq 7$, tends to correspond to that where the viscoelastic model of Squire and Allan (1977) starts to become of comparable

magnitude and slope (Fig. 5). A similar observation could be made based on Fig. 6, although such a transition would be at a larger wave period of $T \approx 10$ s. This would support the observations of Meylan et al. (2018), who argued that there are two dissipative processes of importance, with one dominating for short waves and the other for long waves. Here, these processes are dissipation due to the ice layer and dissipation beneath the sea ice, respectively. The position of transition observed here seems to be determined by the ice thickness through the wave dispersion relationship by the lengthening of the short waves. This point is likely defined by the frequency at which the elastic effects of the ice dominate the modification of the wave speed in the ice (Fox and Haskell, 2001; Collins et al., 2017). A correlation between wave attenuation rates and ice thickness was also observed by Doble et al. (2015) and Rogers et al. (2021), for pancake and broken pack ice, and considered by Yu et al. (2019) more generally for both wave dispersion and dissipation.

Though the model of Sutherland et al. (2019) significantly underestimates the observations in both experiments, by increasing the wave-permitting layer to $\epsilon \approx 0.5$ for the Arctic experiment, and $\epsilon \approx 0.1$ for the Antarctic experiment, the model results fit well to our observations. This raises questions about the physical interpretation of ϵ , which, similar to the viscous ice models, uses an effective viscosity parameter to capture ice-induced wave dissipation. For a solid and continuous ice layer, the interpretation becomes difficult. Sutherland et al. (2019) reason that it is possible that sea ice permeability allows wave-induced pressure gradients within a layer ϵ of the sea ice. Indeed, boundary permeability allows flow penetration across the water–ice interface much like that of coherent turbulent structures at the permeable sediment–water interface (e.g., Voermans et al., 2018), and for large permeability and/or flow-induced shear, boundary permeability can lead to significantly enhanced momentum exchange across the interface and thus an enhanced drag coefficient (or equivalent, the effective viscos-

ity). However, even for a relatively large sea ice permeability of $K = O(10^{-10} \text{ m}^2)$ (e.g., Golden et al., 2007), no significantly enhanced momentum exchange is expected if one would assume the analogy with the sediment–water interface to be valid (Voermans et al., 2018). That is, the pressure gradients induced by the waves propagating under the ice are too weak to drive flow within the porous ice as the resistance of the ice is simply too large. A dissipation process related to ice permeability that might be more plausible is that of brine migration driven by pressure gradients within the ice layer induced by the flexural response of the ice to the waves (Marchenko and Cole, 2017). However, the complexity of this process makes it difficult to identify whether wave energy dissipation by brine migration is an important process in our experiments.

While our observations tend to indicate that boundary layer turbulence and viscoelastic dissipation are dominant dissipative processes in landfast ice in different frequency ranges, one can only be certain of their importance when the mechanical and physical properties of the ice (including the under-ice topography) and details of the turbulent boundary layer under the ice are known. Measuring turbulence under the ice in situ is a complex task, not only because of the challenging environment, but also as the thickness of the wave boundary layer is expected to be small; that is, in landfast ice the boundary layer is expected to be just a few centimeters thick if no extreme roughness formations (such as platelet ice and ice ridges) are present. This complicates the use of acoustic measurement techniques which pose limitations near boundaries due to reflection and low flow velocities, and perhaps optical methods using remotely operated vehicles (ROVs) could provide a solution to this experimental problem (Løken et al., 2021). As opposed to the need to measure the elastic modulus of the ice through mechanical tests, a potential method to identify the elastic modulus in sea ice, at least for a continuous ice sheet, is by estimating wave number through measurements of heave, pitch, and roll (e.g., see Fig. 2). However, independent mechanical tests still need to verify the accuracy of such a method.

Lastly, we believe it is worthwhile to briefly discuss the commonly adopted assumption that the wave attenuation rate can be approximated as linear; that is, the attenuation rate is assumed independent of wave height, or, more specifically, it is assumed independent of wave energy as a function of wave frequency $E(f, x)$ (i.e., see Eqs. 1 and 3). While this is not necessarily a preferred assumption, it is usually forced by the difficulties in measuring the spatial attenuation rate at high spatial resolution, due to either deployment limitations or spatial variability of sea ice properties. In our Arctic experiment, the three ice buoys deployed could provide more insight into the non-linearity of the wave attenuation rate, considering that the ice thickness was measured to be reasonably constant between the buoys. However, only observations of α from the buoy pair furthest apart were shown thus far (i.e., see Fig. 3) as observations from this pair are deemed most ac-

curate. In Fig. 7 the estimated attenuation rates are shown for all three buoy pair combinations. We repeat here that buoys 1, 2, and 3 are located 500, 1100, and 1800 m from the landfast ice edge, respectively. As one would expect, the scatter in the estimated attenuation rates is significantly smaller for the buoy pair furthest apart, 1–3, and largest for buoy pairs 1–2 and 2–3, as attenuation becomes more difficult to measure accurately at such a short distance with the given instrumentation. Nevertheless, while scatter is large, a power law can be reasonably and consistently fitted to the mean estimates of α . The exception to this are at wave frequencies where the distance between the buoy pair becomes of the same order of magnitude as the wave length, and thus the distance between the buoy pair is too short to reliably observe attenuation (the vertical dotted lines in Fig. 7 correspond to the wave period where $\Delta x \approx 3\lambda$, where Δx is the distance between buoy pairs and λ is the wave length). Notably, the wave attenuation rate varies from $f^{2.2}$ at approximately 800 m from the ice edge to $f^{3.0}$ about 1450 m from the landfast ice edge (Fig. 7d). The magnitude of the fitted power laws decreases moving from the landfast ice edge further into the sea ice, substantiating that the wave attenuation rate is indeed dependent on the local wave energy. Moreover, while the overall wave attenuation rate of long waves is weaker than for short waves, their dependence on wave height is stronger. Of course, while these observations seem to substantiate non-linear behavior of wave attenuation in sea ice through its dependence of α on both wave energy and wave length, caution is required in interpreting the observations obtained between pairs 1–2 and 2–3 as the scatter for these pairs exceeds the differences between the mean attenuation rates between the different buoy pairs. As such, to validate these observations, more targeted experiments are necessary.

5 Conclusions

Observations of waves in landfast ice were used to gain insight into the importance and relevance of various wave–ice interactive processes in the attenuation of wave energy in sea ice. Our estimates of the wave number suggest that the dispersion relation in landfast ice is well described by the thin elastic plate assumption. The ability to estimate the wave dispersion relation using a single ice buoy implies that the elastic modulus of landfast ice may be estimated using wave observations. We observe wave attenuation rates in landfast ice to be an order of magnitude larger than in broken ice. This is consistent with current understanding that the wave attenuation rate in sea ice is dominated by whether the ice is broken or unbroken and is strongly determined by the type of sea ice. Results suggest that viscoelastic theory can only explain the observed attenuation rates in landfast ice for short waves, whereas the longwave attenuation rates (and in part the short waves as well) are well described by turbulence and friction-based dissipation models. The wave period de-

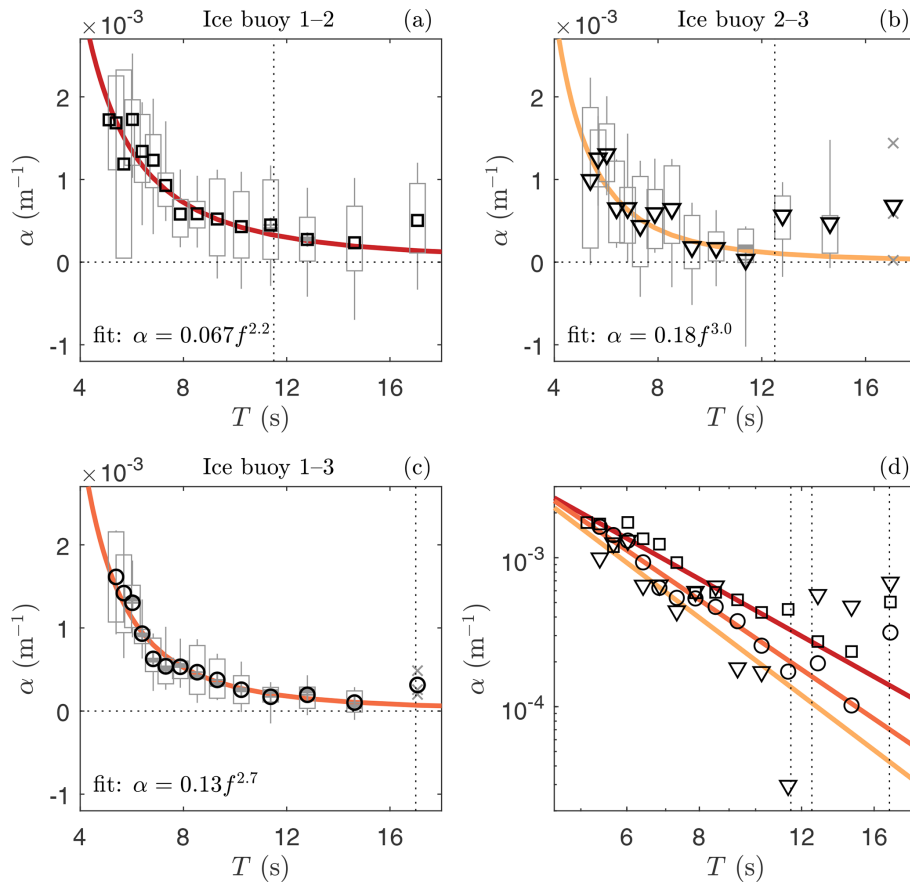


Figure 7. Mean wave attenuation rate α (markers) observed during the Arctic experiment and estimated based on buoy pairs: (a) 1–2, (b) 2–3, and (c) 1–3 (see also Fig. 3a). Ice buoys 1, 2, and 3 are positioned 500, 1100, and 1800 m from the estimated landfast ice edge, respectively. In (a)–(c), boxes identify the 25th and 75th percentiles, and the vertical bars identify the 9th and 91st percentiles. Vertical dotted lines correspond to the wave period where the buoy pair distance is 3 times the wave length. Best fits to the experimental data are provided in color and presented in log-scale in (d).

describing this transition between short and long waves is expected to be dominated by the thickness of the ice. Evaluation of the variability of the wave attenuation with distance from the landfast ice edge substantiates a non-linear dependence of attenuation on wave energy and wave frequency. Specifically, the wave attenuation rates of the longer waves are weaker than for the shorter waves, but their dependence on wave energy is stronger. A general note of caution is that to match the observations to the turbulence and friction models, large-momentum-transfer variables are required which, under the experimental conditions, remain physically unexplained. More comprehensive studies are required to substantiate our conclusions by measuring the local physical and material properties of the ice and flow properties underneath the ice independently, particularly the properties of turbulence.

Appendix A: Wave measurements

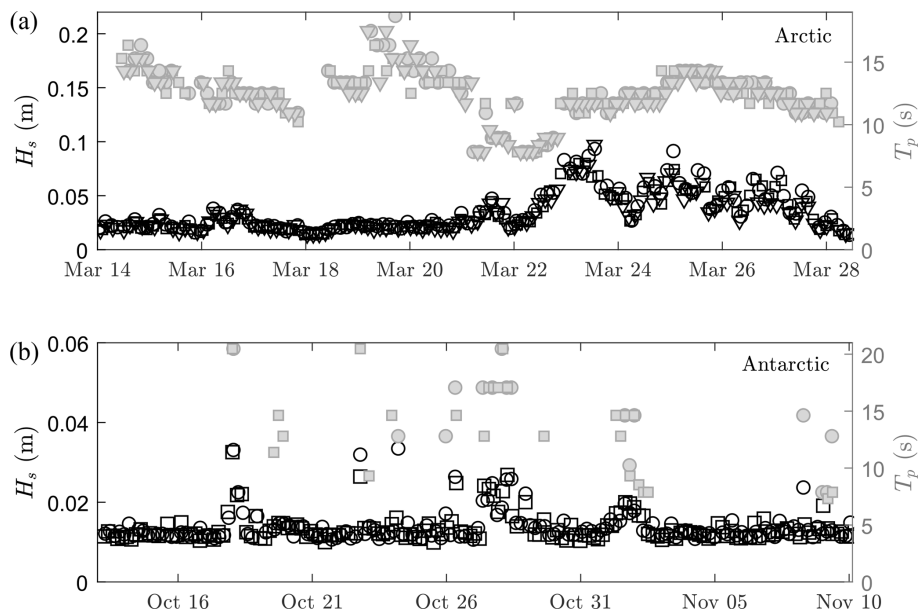


Figure A1. Measured wave height (black) and peak period (gray) during (a) the Arctic experiment (taken from Voermans et al., 2020) and (b) the Antarctic experiment. Note that the noise threshold of H_s is approximately 1.5 cm. Squares, circles, and inverted triangles relate to different instruments within each experiment.

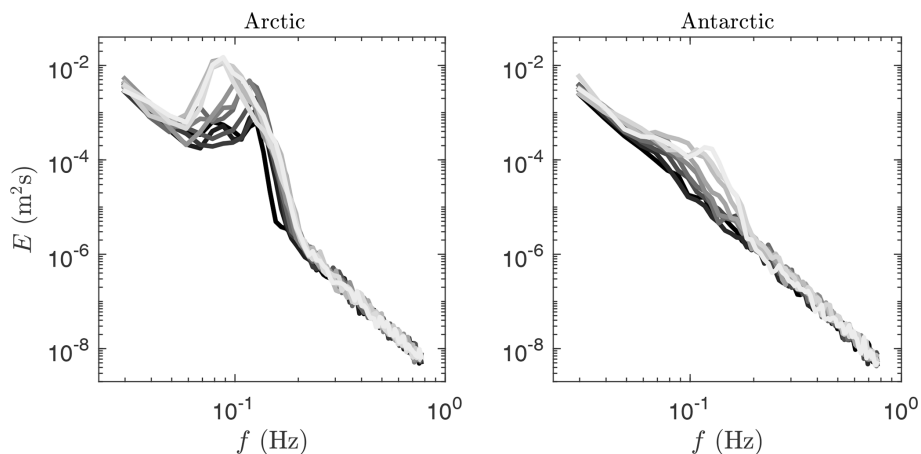


Figure A2. Example spectra derived from the vertical acceleration measured by the ice buoys. For the Arctic, the spectra are from 22 March 2020 (black)–23 March 2020 (light gray). For the Antarctic, the spectra are from 31 October 2020 (black)–2 November 2020 (light gray). For the Antarctic, only a few spectra pass the SNR criterion.

Appendix B: Ice viscosity

B1 Laboratory experiments

Spray ice is formed in the coastal zone near Longyearbyen due to regular floods of water onshore due to semidiurnal tide and waves. The tide height changes between 1 and 2 m depending on the moon phase. Accordingly, the water line moves over the coastal slope and freezes. In addition, sea spray freezes along the coastal slope where it accumulates. As a result, a layer of spray ice with a thickness of 1.5 m was formed along the shoreline to the end of February 2020. The salinity of spray ice was measured from 3.5 to 5.6 ppt. The photographs of vertical and horizontal sections of the spray ice made in polarized light are shown in Fig. B1. The length scale at the left side of the photographs shows length in centimeters. The ice has very fine granular structures with a maximal grain diameter of about 1 mm.

Winter 2020 was very cold in Spitsbergen, and the thickness of sea ice reached 1 m in the Van Mijen Fjord near Cape Amsterdam in March 2020. This ice has columnar structure S_3 with alignment of c axes in the onshore direction and elongation of the columnar grains in the alongshore direction. The photographs of the vertical and horizontal sections of the sea ice made in polarized light are shown in Fig. B2. The yellow strip at the left side of the photographs has a length of 5 cm. The size of columnar grains in the onshore direction is about 2 cm, and the size of columnar grains in the alongshore direction is about 5 cm. The sea ice salinity was measured in the range of 4–6 ppt.

Ice cores taken from spray sea ice and columnar sea ice were used in the laboratory tests on uniaxial compression to calculate elastic and viscous properties of sea ice (Fig. B3a). The length and the diameter of ice cores were respectively 175 and 72 mm. In each test ice cores were subjected to constant compressive load over some time and then unloaded (LU test). The tests were performed in the cold laboratory of The University Centre in Svalbard by the test machine Knekkis. The load was measured by two similar HBM load cells 10 t mounted in the rig and placed on the surface of the ice core (Fig. B3b). Records of the second load cell were synchronized with the records of the Epsilon Tech extensometer, with a 50 mm base, mounted in the middle part of the ice core. Records of the Knekkis load cell were synchronized with the records of vertical displacement of the plate supporting the ice core in the rig.

Deformations recorded by the Epsilon Tech extensometer were usually smaller than deformations calculated from the records of the displacement sensor in the Knekkis. The difference is explained by ice failure effects at the edges of ice cores. We are sure that strains measured by the Epsilon Tech sensor better reproduce the strains in the middle part of ice cores, which are most important for the description of ice rheology.

Examples of test records are shown in Figs. B4–B6. Figures B4a and B5a show records of the stresses versus time in the tests with spray sea ice and columnar sea ice, respectively. The core of spray sea ice was subjected to one LU test with constant compression of about 1 MPa for 10 min. The horizontal core of columnar sea ice was subjected to three consequent LU tests. The duration of each compression was 100 s. In test 1 the stress was about 1.5 MPa, and in tests 2 and 3 the stress was about 1 MPa. Blue, yellow, and green lines correspond to the first, the second, and the third tests. Figures B4b and B5b show records of the strains versus time in the tests. The return of strains after the loads are removed are very visible in the figures. Figure B5b shows accumulation of irreversible strains after each test: the initial strain equals zero on the blue line, the initial strain is higher at the yellow line, and the initial strain is maximal at the green line. Figure B6 shows the normalized strains in the tests versus time after the load is removed. Representative times of the return of delayed strains are estimated at 30 s in the spray ice and 75 s in the columnar ice.

B2 Rheological constants of spray and columnar ice

It is assumed that ice rheology is described by Burgers model consisting of linear combination of Maxwell and Kelvin–Voigt units:

$$\ddot{\epsilon}\tau_2 + \dot{\epsilon} = \frac{\dot{\sigma}}{E_{\text{eff}}} + \dot{\sigma} \frac{\tau_2}{E_1} + \frac{\sigma}{\eta_1}, \quad (\text{B1})$$

where σ and ϵ are stress and strain, and dots above the letters means the time derivatives. Rheological constants are determined by $\tau_2 = \eta_2/E_2$ and $1/E_{\text{eff}} = 1/E_1 + \tau_2/\mu$. Here, E_1 and η_1 are elastic and viscous constants of the Maxwell unit, and E_2 and η_2 are elastic and viscous constants of the Voigt unit.

Acoustic measurements of the speed of longitudinal waves combined with measurements of the natural frequencies of ice beams and discs show that elastic modulus $E_1 \approx 5$ GPa for sea spray ice and for columnar sea ice in the horizontal direction at -5°C (Marchenko et al., 2021). From Fig. B6 it follows that $\tau_2 = 30$ s for sea spray ice and $\tau_2 = 75$ s for columnar sea ice. The rheological constants E_2 , η_1 , and η_2 are found from the approximation of the dependencies shown in Figs. B4b and B5b by the solution of Eq. (B1) obtained with prescribed dependencies of the stress σ from the time shown in Figs. B7 and B8 by thin lines. They are given by the equation

$$\frac{\sigma}{\sigma^*} = 0.5 \left(1 + \tanh \left(100 \left(\frac{t}{t_*} - t_A \right) \right) \right) \frac{\sigma(t_C)}{\sigma^*} - 0.5 \left(1 + \tanh \left(100 \left(\frac{t}{t_*} - t_B \right) \right) \right) \frac{\sigma(t_C)}{\sigma^*}, \quad (\text{B2})$$

where the values t_A , t_B , and t_C correspond to the points A, B, and C shown in Figs. B7a and B8a. Equation (B2) was

adjusted to the stress record in each test. Results of tests 2 and 3 performed with a core of columnar sea ice are very similar. Therefore, only tests 1 and 2 were simulated.

Numerical simulations were performed with dimensionless Eq. (1) derived with representative stress $\sigma^* = 1$ MPa, strain $\epsilon^* = 0.001$, and $t_* = 100$ s. The initial conditions are $\epsilon(0) = \dot{\epsilon}(0) = 0$. The strains calculated from Eq. (B1) with the values of rheological constants shown in Table B1 are shown by thin lines in Figs. B7b and B8b. The thin lines approximate the recorded strains on the segments A, C, and B well.

Table B1. Rheological coefficients of spray sea ice and columnar sea ice.

	E_1 (GPa)	E_2 (GPa)	η_1 (GPa s ⁻¹)	η_2 (GPa s ⁻¹)	μ (GPa s ⁻¹)	E_{eff} (GPa)
Spray ice	5	1.2	176	36	30	0.8
Columnar ice	5	1	55	75	32	0.4
	5	1	83	75	39	0.5

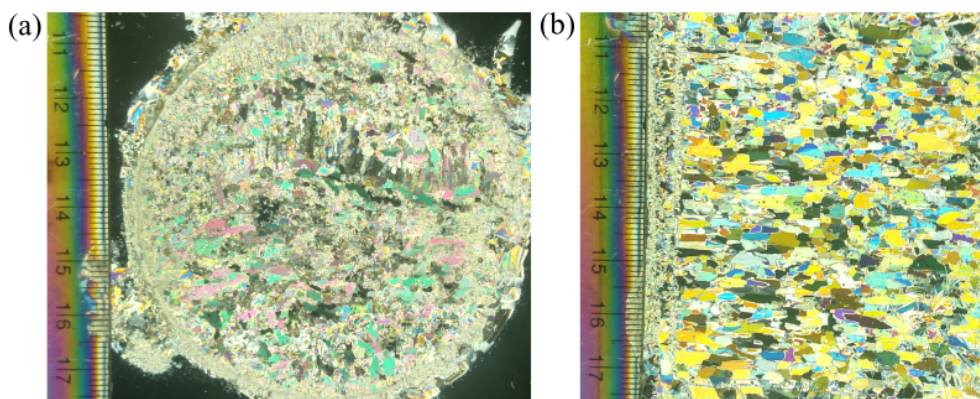


Figure B1. (a) Horizontal and (b) vertical thin sections of spray sea ice.

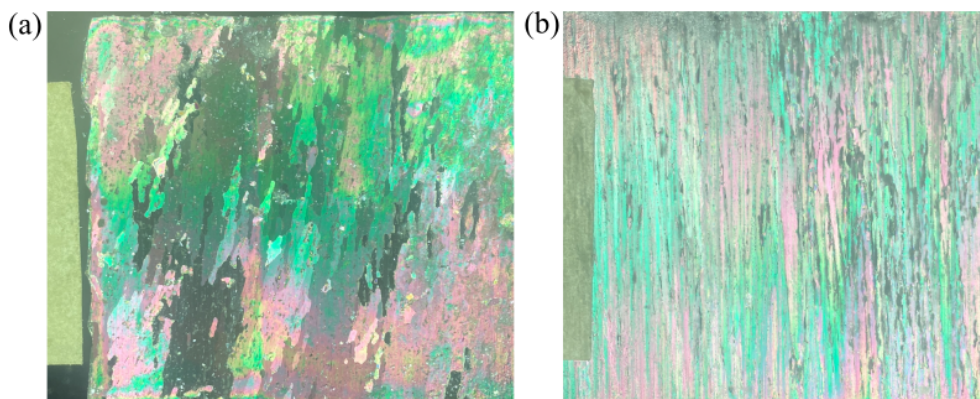


Figure B2. (a) Horizontal and (b) vertical thin sections of columnar sea ice.

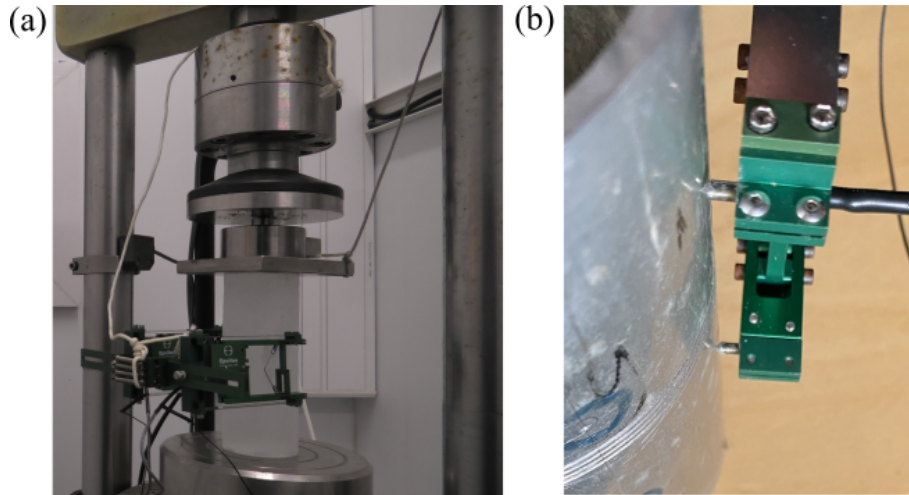


Figure B3. (a) Overview of uniaxial compression test. (b) Mounting of strain sensor on a sample.

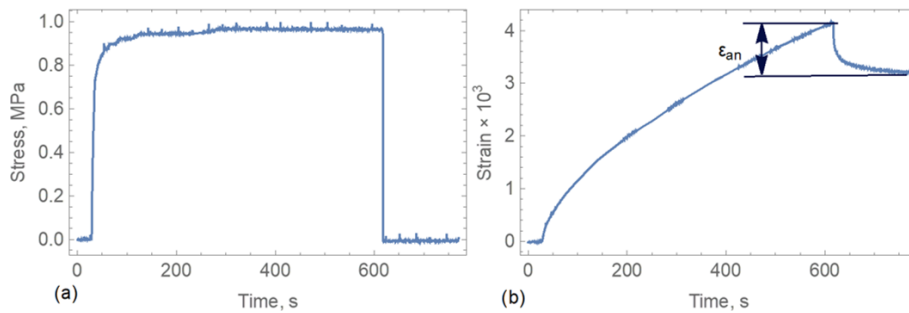


Figure B4. Stress and strain versus time in LU test with an ice core of spray ice (ice temperature is 5 °C).

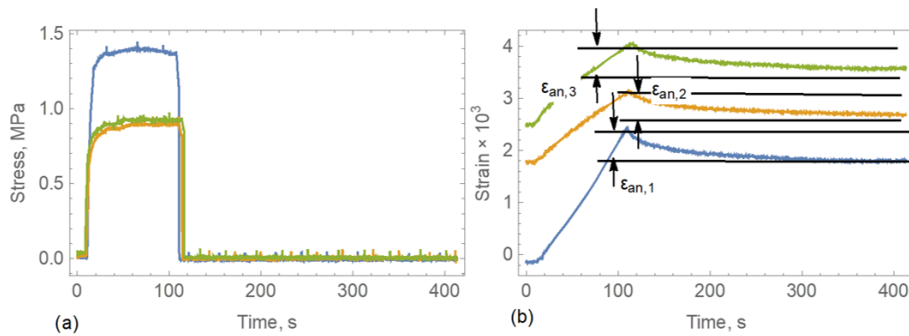


Figure B5. Stress and strain versus time in three LU tests performed with the same core of columnar ice (ice temperature is 5 °C).

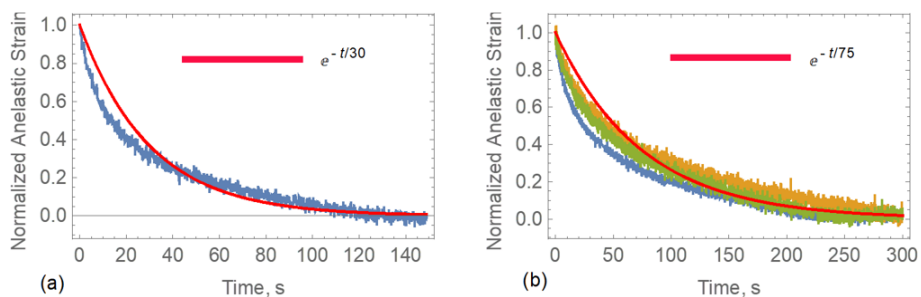


Figure B6. Normalized strain versus time in LU tests performed with (a) spray and (b) columnar sea ice cores (ice temperature is 5 °C).

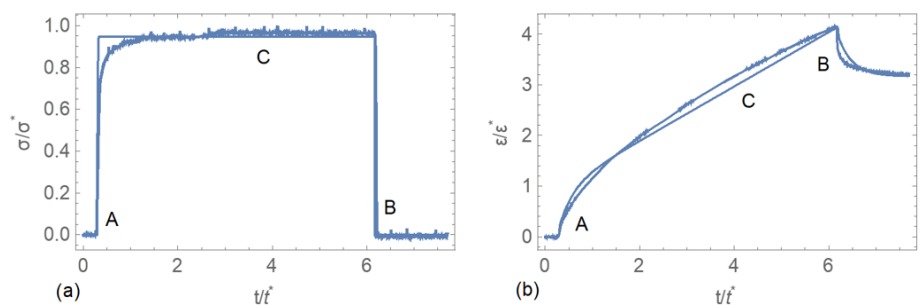


Figure B7. (a) Dimensionless stress and (b) normalized strains versus dimensionless time. Thick and thin lines correspond to measured and simulated quantities, respectively. LU test with a core of spray sea ice.

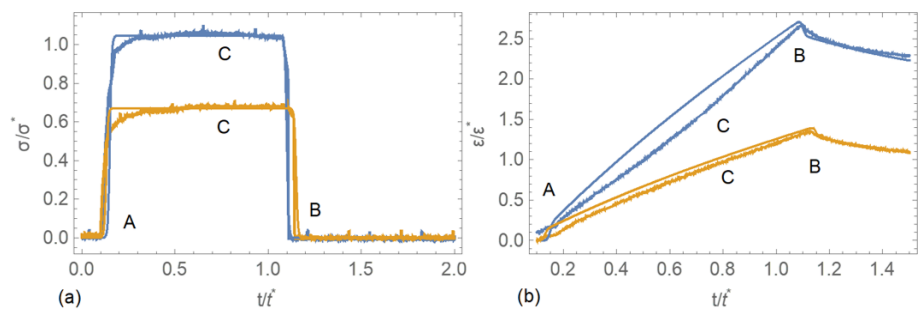


Figure B8. (a) Dimensionless stress and (b) normalized strains versus dimensionless time. Thick and thin lines correspond to measured and simulated quantities, respectively. Blue and yellow lines correspond to two LU tests with a core of columnar sea ice.

Appendix C: Models

An overview of the different wave dispersion and dissipation models used in this study is provided here in order as presented in Fig. 5. For brevity, models are presented with limited context, and the reader is referred to the model references for further details.

C1 Squire and Allan (1977)

The simplified viscoelastic model of Squire and Allan (1977) can be written as (Li et al., 2015; Sree et al., 2018)

$$(\omega^2 - Qgk \tanh kH) = 0, \quad (C1)$$

$$Q = \frac{(G - i\omega\rho_i\nu)h^3}{6g\rho_w(1-\theta)}k^4 - \frac{\rho_i h \omega^2}{\rho_w g} + 1, \quad (C2)$$

where θ is the Poisson ratio, here taken as 0.3, and the shear modulus $G = Y/(2(1+\theta))$. We note that k represents the complex wave number, $k = k_r + ik_i$, such that

$$\alpha = 2k_i. \quad (C3)$$

C2 Marchenko et al. (2020)

$$\omega^2 = k \tanh(kH) \left(g + \frac{E_1 h^3 k^4}{12\rho_w} \right) \quad (C4)$$

$$\alpha = \frac{E_1 h^3 k^4}{24\rho_w (g + E_1 h^3 k^4 / 12\rho_w)} \frac{E_1}{\mu_i c_g} \quad (C5)$$

Here μ_i is the ice viscosity. In this study, we used $E_1 = Y$.

C3 Sutherland et al. (2019)

$$\alpha = \Delta_0 \epsilon h k^2 \quad (C6)$$

Here in this study $\Delta_0 = 1$, i.e., a no-slip boundary condition. For a continuous ice sheet, it is expected that ϵ is small, and thus here we choose $\epsilon = 0.01$. For an ice thickness of $h = 0.35$ m, this corresponds to a highly viscous layer of 3.5 mm.

C4 Marchenko and Cole (2017)

The spatial attenuation rate is calculated according to the model of Marchenko and Cole (2017) by the formula

$$\alpha = \frac{Y^2 k^5 \tanh(kH)}{4c_g \rho_w \mu_w \omega^2 (1-\theta^2)^2} \int_0^h \frac{K}{\phi} dz, \quad (C7)$$

where K is the permeability of the ice in square meters, μ_w is the dynamic viscosity of the brine (taken here as $1.5 \times 10^{-3} \text{ Pa s}^{-1}$), and ϕ is the liquid brine volume content calculated with the formula $\phi = \sigma_{si}(49.185/|T| + 0.532)$ (Frankenstein and Garner, 1967), where σ_{si} is the sea ice

salinity, here taken as 10 ppt. Sea ice permeability is estimated by the formula $K = K_0 \exp(15\sqrt{\phi})$ (Zhu et al., 2006). We estimate α assuming that the sea ice temperature varies linearly from -2°C at the ice bottom ($z = 0$) to -25° at the ice surface ($z = h$) according to $T = -2 - 23z/h$.

C5 Liu and Mollo-Christensen (1988)

$$\omega^2 = \frac{gk_r + Bk_r^5}{\coth(k_r H) + k_r M} \quad (C8)$$

$$c_g = \frac{g + (5 + 4k_r M) Bk_r^4}{2\omega(1 + k_r M)^2} \quad (C9)$$

$$\alpha = \frac{\sqrt{\nu\omega}k_r}{c_g \sqrt{2}(1 + k_r M)} \quad (C10)$$

Here $B = Yh^3/\rho_w 12(1-\theta^2)$ and $M = h\rho_i/\rho_w$, and g is the gravitational acceleration, H is the water depth, Y is the elastic modulus of the ice, ρ_w and ρ_i are the densities of water and ice, respectively, θ is the Poisson ratio, and h is the ice thickness. Note that the contribution of ice compression has been ignored here.

C6 Kohout et al. (2011)

$$\alpha = 2H_s C_D k^2 \quad (C11)$$

Here C_D is the under-ice drag coefficient.

C7 Stopa et al. (2016)

Considering a fully turbulent boundary layer under the ice and assuming the analogy between the wave–ice boundary layer and the wave bottom boundary layer holds, the wave attenuation rate may be given by

$$\alpha = f_w \frac{\omega^2 u_{\text{orb}}}{g c_g}, \quad (C12)$$

where $u_{\text{orb}} = \omega a_0$ is the wave orbital motion, a is the wave amplitude and taken as $H_s/2$, and f_w is the friction factor for which we here use the simplified model of Soulsby (1997):

$$f_w = 1.39 \left(\frac{a}{k_s/30} \right)^{-0.52}, \quad (C13)$$

$$f_{w,\text{max}} = 0.3. \quad (C14)$$

Here, k_s is the Nikuradse roughness height. We refer to Stopa et al. (2016) for the WaveWatchIII source code for more details on Eq. (C12).

Data availability. Data of the Arctic and Antarctic experiment are available at the Australian Antarctic Data Centre, <https://doi.org/10.4225/15/590173acc61c9> (Voermans, 2020) and <https://doi.org/10.26179/2drt-2j12> (Voermans, 2021a), respectively. Data to replicate Figs. 2, 3, and 7 are available at <https://doi.org/10.5281/zenodo.5568527> (Voermans, 2021b).

Author contributions. JJV and AVB conceptualized the experiment. JV and JR constructed instrumentation. KF and IR deployed and retrieved instrumentation. AM retrieved ice cores from the Arctic and designed and performed laboratory experiments on ice cores. QL and JL assisted in the modeling. AVB and AM administered the project. JJV and AM prepared the original draft. JJV, QL, AM, JR, PH, TW, TN, and TK discussed results and edited the manuscript. All authors reviewed the manuscript.

Competing interests. The contact author has declared that neither they nor their co-authors have any competing interests.

Disclaimer. Publisher's note: Copernicus Publications remains neutral with regard to jurisdictional claims in published maps and institutional affiliations.

Acknowledgements. We acknowledge the use of imagery from the NASA WorldView application (<https://worldview.earthdata.nasa.gov/>, last access: 17 April 2021), part of the NASA Earth Observing System Data and Information System (EOSDIS). Authors would like to thank Flynn Jackman and the rest of the team at Casey Station, Antarctica, for their assistance in deploying instrumentation and collecting ice samples. Data collection in Grønfyorden, Svalbard, was conducted within the expedition “Spitsbergen-2020” organized by the Russian Scientific Arctic Expedition on Spitsbergen Archipelago (RAE-S), AARI. Joey J. Voermans, Qingxiang Liu, and Alexander V. Babanin acknowledge support from the Joyce Lambert Antarctic Research Fund and the US Office of Naval Research grant N62909-20-1-2080. Joey J. Voermans, Alexander V. Babanin, and Petra Heil were supported by the Australian Antarctic Program under project 4593 and Petra Heil under project 4506. Aleksey Marchenko acknowledges support from “Arctic Engineering in Changing Climate” (RCN, N 274951). The International Space Science Institute (Bern, Switzerland) is thanked for supporting scientific collaborations of this study through project “Multi-Sensor Observations of Antarctic Sea Ice and its Snow Cover” (#501). Joey J. Voermans, Jean Rabault, Kirill Filchuk, Aleksey Marchenko, Takuji Waseda, and Alexander V. Babanin acknowledge the support of the Research Council of Norway through the SFI SIB project. Jean Rabault was supported in the context of the DOFI project (University of Oslo, grant no. 280625). Lastly, the authors are grateful for the comments and feedback provided by the anonymous reviewers.

Financial support. This research has been supported by the Office of Naval Research (grant no. N62909-20-1-2080) and the Australian Antarctic Division (grant nos. 4593 and 4506).

Review statement. This paper was edited by Yevgeny Aksenov and reviewed by two anonymous referees.

References

- Ardhuin, F., Sutherland, P., Doble, M., and Wadhams, P.: Ocean waves across the Arctic: Attenuation due to dissipation dominates over scattering for periods longer than 19 s, *Geophys. Res. Lett.*, 43, 5775–5783, 2016.
- Ardhuin, F., Otero, M., Merrifield, S., Grouazel, A., and Terrill, E.: Ice breakup controls dissipation of wind waves across Southern Ocean Sea Ice, *Geophys. Res. Lett.*, 47, e2020GL087699, <https://doi.org/10.1002/2016GL068204>, 2020.
- Cheng, S., Rogers, W. E., Thomson, J., Smith, M., Doble, M. J., Wadhams, P., Kohout, A. L., Lund, B., Persson, O. P. G., Collins III, C. O., Ackley, S. F., Montiel, F., and Shen, H. H.: Calibrating a viscoelastic sea ice model for wave propagation in the Arctic fall marginal ice zone, *J. Geophys. Res.-Oceans*, 122, 8770–8793, 2017.
- Cheng, S., Stopa, J., Ardhuin, F., and Shen, H. H.: Spectral attenuation of ocean waves in pack ice and its application in calibrating viscoelastic wave-in-ice models, *The Cryosphere*, 14, 2053–2069, <https://doi.org/10.5194/tc-14-2053-2020>, 2020.
- Collins, C., Doble, M., Lund, B., and Smith, M.: Observations of surface wave dispersion in the marginal ice zone, *J. Geophys. Res.-Oceans*, 123, 3336–3354, 2018.
- Collins, C. O., Rogers, W. E., and Lund, B.: An investigation into the dispersion of ocean surface waves in sea ice, *Ocean Dynam.*, 67, 263–280, 2017.
- Collins III, C. O., Rogers, W. E., Marchenko, A., and Babanin, A. V.: In situ measurements of an energetic wave event in the Arctic marginal ice zone, *Geophys. Res. Lett.*, 42, 1863–1870, 2015.
- Doble, M. J., De Carolis, G., Meylan, M. H., Bidlot, J.-R., and Wadhams, P.: Relating wave attenuation to pancake ice thickness, using field measurements and model results, *Geophys. Res. Lett.*, 42, 4473–4481, 2015.
- Fox, C. and Haskell, T. G.: Ocean wave speed in the Antarctic marginal ice zone, *Ann. Glaciol.*, 33, 350–354, 2001.
- Frankenstein, G. and Garner, R.: Equations for determining the brine volume of sea ice from -0.5° to -22.9° C, *J. Glaciol.*, 6, 943–944, 1967.
- Golden, K. M., Eicken, H., Heaton, A., Miner, J., Pringle, D., and Zhu, J.: Thermal evolution of permeability and microstructure in sea ice, *Geophys. Res. Lett.*, 34, L16501, <https://doi.org/10.1029/2007GL030447>, 2007.
- Herman, A.: Spectral wave energy dissipation due to under-ice turbulence, *J. Phys. Oceanogr.*, 51, 1177–1186, 2021.
- Herman, A., Cheng, S., and Shen, H. H.: Wave energy attenuation in fields of colliding ice floes – Part 2: A laboratory case study, *The Cryosphere*, 13, 2901–2914, <https://doi.org/10.5194/tc-13-2901-2019>, 2019.
- Kodaira, T., Waseda, T., Nose, T., Sato, K., Inoue, J., Voermans, J., and Babanin, A.: Observation of on-ice wind waves under grease ice in the western Arctic Ocean, *Polar Sci.*, 27, 100567, <https://doi.org/10.1016/j.polar.2020.100567>, 2020.
- Kohout, A. and Williams, M.: Waves in-ice observations made during the SIPEX II voyage of the Aurora Australis, 2012, Australian Antarctic Data Centre [data set], <https://doi.org/10.4225/15/53266BEC9607F>, updated 2015, 2013.
- Kohout, A. L., Meylan, M. H., and Plew, D. R.: Wave attenuation in a marginal ice zone due to the bottom roughness of ice floes, *Ann. Glaciol.*, 52, 118–122, 2011.

- Kovalev, D. P., Kovalev, P. D., and Squire, V. A.: Crack formation and breakout of shore fast sea ice in Mordvinova Bay, south-east Sakhalin Island, *Cold Reg. Sci. Technol.*, 175, 103082, <https://doi.org/10.1016/j.coldregions.2020.103082>, 2020.
- Kuik, A., Van Vledder, G. P., and Holthuijsen, L.: A method for the routine analysis of pitch-and-roll buoy wave data, *J. Phys. Oceanogr.*, 18, 1020–1034, 1988.
- Li, J., Mondal, S., and Shen, H. H.: Sensitivity analysis of a viscoelastic parameterization for gravity wave dispersion in ice covered seas, *Cold Reg. Sci. Technol.*, 120, 63–75, 2015.
- Li, J., Kohout, A. L., Doble, M. J., Wadhams, P., Guan, C., and Shen, H. H.: Rollover of apparent wave attenuation in ice covered seas, *J. Geophys. Res.-Oceans*, 122, 8557–8566, 2017.
- Lindgren, S.: Effect of Temperature Increase of Ice Pressure, Royal Institute of Technology, Stockholm, Sweden, 1986.
- Liu, A. K. and Mollo-Christensen, E.: Wave propagation in a solid ice pack, *J. Phys. Oceanogr.*, 18, 1702–1712, 1988.
- Liu, Q., Rogers, W. E., Babanin, A., Li, J., and Guan, C.: Spectral modeling of ice-induced wave decay, *J. Phys. Oceanogr.*, 50, 1583–1604, 2020.
- Løken, T. K., Ellevold, T. J., de la Torre, R. G. R., Rabault, J., and Jensen, A.: Bringing optical fluid motion analysis to the field: a methodology using an open source ROV as camera system and rising bubbles as tracers, *Meas. Sci. Technol.*, 32, 095302, <https://doi.org/10.1088/1361-6501/abf09d>, 2021.
- Lu, P., Li, Z., Cheng, B., and Leppäranta, M.: A parameterization of the ice-ocean drag coefficient, *J. Geophys. Res.-Oceans*, 116, C07019, <https://doi.org/10.1029/2010JC006878>, 2011.
- Marchenko, A. and Cole, D.: Three physical mechanisms of wave energy dissipation in solid ice, in: Proceedings of the International Conference on 11 June 2017, Busan, South Korea, 2017.
- Marchenko, A., Rabault, J., Sutherland, G., Collins, C. O., Wadhams, P., and Chumakov, M.: Field observations and preliminary investigations of a wave event in solid drift ice in the Barents Sea, in: Proceedings-International Conference on Port and Ocean Engineering under Arctic Conditions, Port and Ocean Engineering under Arctic Conditions, 11–16 June 2017, Busan, South Korea 2017.
- Marchenko, A., Haase, A., Jensen, A., Lishman, B., Rabault, J., Evers, K., Shortt, M., and Thiel, T.: Elasticity and viscosity of ice measured in the experiment on wave propagation below the ice in HSVA ice tank, in: 25th IAHR International Symposium on Ice, The International Association for Hydro-Environment Engineering and Research, 23–27 November 2020, Trondheim, Norway, 2020.
- Marchenko, A., Haase, A., Jensen, A., Lishman, B., Rabault, J., Evers, K.-U., Shortt, M., and Thiel, T.: Laboratory Investigations of the Bending Rheology of Floating Saline Ice and Physical Mechanisms of Wave Damping In the HSVA Hamburg Ship Model Basin Ice Tank, *Water*, 13, 1080, <https://doi.org/10.3390/w13081080>, 2021.
- McPhee, M. G. and Martinson, D. G.: Turbulent mixing under drifting pack ice in the Weddell Sea, *Science*, 263, 218–221, 1994.
- Meylan, M. H., Bennetts, L. G., Mosig, J., Rogers, W., Doble, M., and Peter, M. A.: Dispersion relations, power laws, and energy loss for waves in the marginal ice zone, *J. Geophys. Res.-Oceans*, 123, 3322–3335, 2018.
- Nelli, F., Bennetts, L. G., Skene, D. M., and Toffoli, A.: Water wave transmission and energy dissipation by a floating plate in the presence of overwash, *J. Fluid Mech.*, 889, A19, <https://doi.org/10.1017/jfm.2020.75>, 2020.
- Rabault, J., Sutherland, G., Jensen, A., Christensen, K. H., and Marchenko, A.: Experiments on wave propagation in grease ice: combined wave gauges and particle image velocimetry measurements, *J. Fluid Mech.*, 864, 876–898, 2019.
- Rabault, J., Sutherland, G., Gundersen, O., Jensen, A., Marchenko, A., and Breivik, Ø.: An open source, versatile, affordable waves in ice instrument for scientific measurements in the Polar Regions, *Cold Reg. Sci. Technol.*, 170, 102955, <https://doi.org/10.1016/j.coldregions.2019.102955>, 2020.
- Rogers, W. E., Thomson, J., Shen, H. H., Doble, M. J., Wadhams, P., and Cheng, S.: Dissipation of wind waves by pancake and frazil ice in the autumn Beaufort Sea, *J. Geophys. Res.-Oceans*, 121, 7991–8007, 2016.
- Rogers, W. E., Meylan, M. H., and Kohout, A. L.: Estimates of spectral wave attenuation in Antarctic sea ice, using model/data inversion, *Cold Reg. Sci. Technol.*, 182, 103198, <https://doi.org/10.1016/j.coldregions.2020.103198>, 2021.
- Shen, H. H.: Modelling ocean waves in ice-covered seas, *Appl. Ocean Res.*, 83, 30–36, 2019.
- Soulsby, R.: Dynamics of marine sands, T. Telford, London, 1997.
- Squire, V. A.: A fresh look at how ocean waves and sea ice interact, *Philos. T. Roy. Soc. A*, 376, 20170342, <https://doi.org/10.1098/rsta.2017.0342>, 2018.
- Squire, V. A.: Ocean wave interactions with sea ice: a reappraisal, *Annu. Rev. Fluid Mech.*, 52, 37–60, 2020.
- Squire, V. A. and Allan, A.: Propagation of flexural gravity waves in sea ice, in: Vol. 2, Symposium on Sea Ice Processes and Models, Proceedings, 6–9 September 1977, University of Washington, Seattle, USA, 1977.
- Squire, V. A., Robinson, W. H., Meylan, M., and Haskell, T. G.: Observations of flexural waves on the Erebus Ice Tongue, McMurdo Sound, Antarctica, and nearby sea ice, *J. Glaciol.*, 40, 377–385, 1994.
- Sree, D. K., Law, A. W.-K., and Shen, H. H.: An experimental study on gravity waves through a floating viscoelastic cover, *Cold Reg. Sci. Technol.*, 155, 289–299, 2018.
- Stopa, J. E., Ardhuin, F., and Girard-Ardhuin, F.: Wave climate in the Arctic 1992–2014: seasonality and trends, *The Cryosphere*, 10, 1605–1629, <https://doi.org/10.5194/tc-10-1605-2016>, 2016.
- Sutherland, G. and Rabault, J.: Observations of wave dispersion and attenuation in landfast ice, *J. Geophys. Res.-Oceans*, 121, 1984–1997, 2016.
- Sutherland, G., Rabault, J., Christensen, K. H., and Jensen, A.: A two layer model for wave dissipation in sea ice, *Appl. Ocean Res.*, 88, 111–118, 2019.
- Tabata, T.: Studies on visco-elastic properties of sea ice, in: Arctic Sea Ice, vol. 598, US National Academy of Sciences & National Research Council, Washington, DC, 139–147, 1958.
- Thomson, J., Ackley, S., Girard-Ardhuin, F., Ardhuin, F., Babanin, A., Boutin, G., Brozena, J., Cheng, S., Collins, C., Doble, M., Fairall, C., Guest, P., Gebhardt, C., Gemmrich, J., Graber, H. C., Holt, B., Lehner, S., Lund, B., Meylan, M. H., Maksym, T., Montiel, F., Perrie, W., Persson, O., Rainville, L., Rogers, W. E., Shen, H., Shen, H., Squire, V., Stammerjohn, S., Stopa, J., Smith, M. M., Sutherland, P., and Wadhams, P.: Overview of the arctic sea state and boundary layer physics program, *J. Geophys. Res.-Oceans*, 123, 8674–8687, 2018.

- Thomson, J., Hošeková, L., Meylan, M. H., Kohout, A. L., and Kumar, N.: Spurious rollover of wave attenuation rates in sea ice caused by noise in field measurements, *J. Geophys. Res.-Oceans*, 126, e2020JC016606, <https://doi.org/10.1029/2020JC016606>, 2021.
- Timco, G. and Weeks, W.: A review of the engineering properties of sea ice, *Cold Reg. Sci. Technol.*, 60, 107–129, 2010.
- Toffoli, A., Bennetts, L. G., Meylan, M. H., Cavaliere, C., Alberello, A., Elsnaß, J., and Monty, J. P.: Sea ice floes dissipate the energy of steep ocean waves, *Geophys. Res. Lett.*, 42, 8547–8554, 2015.
- Voermans, J.: Wave–Ice interactions and ice break-up observations in the Southern Ocean, 2020, Australian Antarctic Data Centre [data set], <https://doi.org/10.4225/15/590173acc61c9>, 2020.
- Voermans, J.: Wave–ice interactions collected on landfast ice near Casey Station, 2020, Australian Antarctic Data Centre [data set], <https://doi.org/10.26179/2drt-2j12>, 2021a.
- Voermans, J.: Data for “Wave dispersion and dissipation in landfast ice: comparison of observations against models”, Zenodo [data set], <https://doi.org/10.5281/zenodo.5568527>, 2021b.
- Voermans, J., Babanin, A., Thomson, J., Smith, M., and Shen, H.: Wave attenuation by sea ice turbulence, *Geophys. Res. Lett.*, 46, 6796–6803, 2019.
- Voermans, J. J., Ghisalberti, M., and Ivey, G. N.: A model for mass transport across the sediment–water interface, *Water Resour. Res.*, 54, 2799–2812, 2018.
- Voermans, J. J., Rabault, J., Filchuk, K., Ryzhov, I., Heil, P., Marchenko, A., Collins III, C. O., Dabboor, M., Sutherland, G., and Babanin, A. V.: Experimental evidence for a universal threshold characterizing wave-induced sea ice break-up, *The Cryosphere*, 14, 4265–4278, <https://doi.org/10.5194/tc-14-4265-2020>, 2020.
- Wadhams, P., Squire, V. A., Goodman, D. J., Cowan, A. M., and Moore, S. C.: The attenuation rates of ocean waves in the marginal ice zone, *J. Geophys. Res.-Oceans*, 93, 6799–6818, 1988.
- Wang, R. and Shen, H. H.: Gravity waves propagating into an ice-covered ocean: A viscoelastic model, *J. Geophys. Res.-Oceans*, 115, C06024, <https://doi.org/10.1029/2009JC005591>, 2010.
- Weber, J. E.: Wave attenuation and wave drift in the marginal ice zone, *J. Phys. Oceanogr.*, 17, 2351–2361, 1987.
- Yu, J., Rogers, W. E., and Wang, D. W.: A Scaling for Wave Dispersion Relationships in Ice-Covered Waters, *J. Geophys. Res.-Oceans*, 124, 8429–8438, 2019.
- Zhu, J., Jabini, A., Golden, K., Eicken, H., and Morris, M.: A network model for fluid transport through sea ice, *Ann. Glaciol.*, 44, 129–133, 2006.